fire

MDPI

Article

The Preparation and Performance Study of Organic–Inorganic Nanocomposite Intumescent Fire-Retardant Coatings

Youhao Xie [1,2], Wenjie Wei [3], Liangyuan Qi [1], Weiyi Xing [1,*] and Yuan Hu [1,*]

[1] State Key Laboratory of Fire Science, University of Science and Technology of China, Hefei 230026, China; xyh@chzu.edu.cn (Y.X.); lyq8911@mail.ustc.edu.cn (L.Q.)
[2] School of Mechanical and Electrical Engineering, Chuzhou University, Chuzhou 239000, China
[3] School of Safety Science and Engineering, Anhui Jianzhu University, Hefei 230601, China; wwj0717@stu.ahjzu.edu.cn
* Correspondence: xingwy@ustc.edu.cn (W.X.); yuanhu@ustc.edu.cn (Y.H.); Tel.: +86-13875209863 (W.X.)

Abstract

The issue of thermal runaway in power batteries of new-energy vehicles occurs frequently, posing a serious threat to life and property safety. This study aims to develop a high-performance fire-proof coating to address this problem. Specifically, the research focused on constructing an organic-inorganic composite intumescent fire-resistant coating, with modified halloysites (Ti-HNTs) serving as the key component. In this coating system, the intumescent flame-retardant (IFR) system and Ti-HNTs were employed as the organic and inorganic components, respectively, while water-based epoxy resin emulsion was selected as the matrix material. Through the utilization of XPS, FTIR, and SEM techniques, it was verified that the Ti-HNTs were successfully modified and integrated well with the coating matrix. Following further optimization of the Ti-HNTs proportion and coating thickness, it was determined that the coating containing 4% Ti-HNTs with a designed thickness of 1.5 mm exhibited the optimal fire-proofing performance. In the fire-resistance experiment, after 10 min of testing, the temperature of this coating could reach a minimum of 215.9 °C. Compared to the control group, its heat-insulation effect was enhanced by 49.4%, with an expansion multiplier of 37.7 and a maximum smoke density of 22.55. These results were significantly superior to those of the control group without the addition of Ti-HNTs. SEM analysis indicated that the coating could form a uniform and dense carbon layer, with an inner surface featuring a honeycomb-bubble structure. This SEM-analyzed Ti-HNTs-modified fire-proof coating demonstrated excellent fire resistance and thermal-isolation effects in new-energy vehicle batteries, thus providing reliable fire protection for the batteries. Additionally, impact-resistance tests revealed that the coating could withstand a simulated battery pressure-relief impact without penetration, maintaining its structural integrity and thermal-barrier function. This further validated its reliability for battery fire protection.

Keywords: fire-retardant coating; composite coating; modified halloysite; new energy vehicle battery

Check for updates

Academic Editor: Siqi Huo

Received: 25 May 2026
Revised: 29 June 2026
Accepted: 17 July 2026
Published: 21 July 2026

Copyright: © 2026 by the authors. Licensee MDPI, Basel, Switzerland. This article is an open access article distributed under the terms and conditions of the Creative Commons Attribution (CC BY) license.

1. Introduction

The rapid growth of electric vehicles (EVs) has become a global trend driven by world-wide carbon neutrality goals and transportation electrification. Major markets including Europe, North America and the Asia–Pacific region have all maintained sustained high growth in EV production and sales in recent years, and battery thermal safety has become

a common technical challenge faced by the global EV industry [1,2]. As the world's largest EV market, China has witnessed a continuous increase in battery-related fire accidents in recent years. Thermal runaway triggered by overcharging, mechanical abuse, or internal short circuits may rapidly propagate within battery modules, resulting in fire or explosion and posing serious threats to life and property [3–6]. In addition to intense heat release, thermal runaway is usually accompanied by the emission of combustible gases and toxic smoke, which further aggravate fire hazards and increase rescue difficulty [7–9]. Therefore, improving the fire safety of lithium-ion battery systems has become a major research focus worldwide.

With the rapid expansion of the global electric vehicle (EV) market, ensuring the safety of lithium-ion batteries has become a major concern for both academia and industry. According to the International Energy Agency (IEA), global EV sales exceeded 17 million units in 2024, accounting for more than 20% of new vehicle sales worldwide, highlighting the increasing importance of battery safety in the global transportation sector [10]. In recent years, extensive efforts have been devoted worldwide to developing passive thermal protection technologies capable of mitigating thermal runaway propagation. Representative approaches include intumescent coatings, ceramic-based thermal barriers, aerogel composites, phase-change materials, and multifunctional nanocomposite coatings, all of which aim to delay heat transfer and maintain the structural integrity of battery modules under fire conditions. Significant progress has been achieved in the United States, Germany, Japan, and South Korea, where research institutions and battery manufacturers have continuously optimized fire-protection materials and battery thermal management strategies to improve battery safety and reliability [2,7,11]. In parallel with academic research, technological innovation has also been reflected in rapidly increasing patent activities. Searches of international patent databases, including Google Patents, WIPO PATENTSCOPE, and Espacenet, indicate a continuous increase in patent applications related to battery thermal barrier materials, fire-resistant coatings, ceramic insulation systems, and multifunctional battery-pack protection technologies over the past decade. Despite these advances, many existing technologies still suffer from limited thermal insulation efficiency during prolonged fire exposure, insufficient coating durability, or complicated fabrication processes. Therefore, developing environmentally friendly waterborne fire-resistant coatings with excellent thermal insulation, mechanical robustness, and long-term stability remains an important research direction for next-generation lithium-ion battery thermal protection [12].

From the perspective of industrial technology layout, flame-retardant thermal protection materials for power batteries have become a research and development hotspot in both academia and industry around the world, and relevant technical solutions and patent achievements are continuously emerging.

To suppress battery thermal runaway and its propagation, extensive efforts have been devoted to battery thermal management systems, separator modification, flame-retardant electrolytes, phase-change materials, aerogel insulation, and external fire-protection technologies [13–17]. The mainstream technical solutions for battery thermal protection are compared in Table 1.

Table 1. Comparison of mainstream flame-retardant strategies for battery thermal protection.

Strategy	*Typical Mechanism*	*Advantages*	*Limitations*
Flame-retardant electrolyte	Inhibits electrolyte combustion	High intrinsic safety	High cost, reduced cycle performance
Phase change material	Latent heat absorption	High heat storage density	Slow heat dissipation, easy to leak

Table 1. *Cont.*

Strategy	*Typical Mechanism*	*Advantages*	*Limitations*
Aerogel insulation	Nanopore thermal barrier	Excellent heat insulation	Brittle, poor impact resistance
Intumescent coating	Expanded char insulation	Lightweight, low cost, easy construction	Char layer integrity under impact needs improvement

Battery thermal management and separator modification can effectively delay temperature rise and improve the intrinsic safety of battery cells [18–20]. Meanwhile, phase-change materials and aerogel insulation reduce heat transfer between adjacent cells through heat absorption and thermal insulation mechanisms [21–23]. Although these approaches can effectively delay heat accumulation or reduce flame propagation, most of them are designed for internal battery thermal management and cannot provide direct protection against external fire exposure [24,25]. In contrast, intumescent fire-retardant coatings can rapidly expand under high temperatures to form a thermally insulating char layer, thereby effectively reducing heat transfer and improving fire resistance. Consequently, they have attracted increasing attention as a promising external protection strategy for lithium-ion battery systems, especially for battery module housings and high-voltage cable sheaths [22–25].

Natural halloysite nanotubes (HNTs) possess a unique hollow tubular structure, high specific surface area, abundant surface hydroxyl groups, and good thermal stability, making them attractive inorganic reinforcements for fire-retardant coatings [26]. Their tubular morphology can effectively reinforce the expanded char layer and improve its thermal insulation performance during combustion. However, pristine HNTs exhibit limited compatibility with organic polymer matrices, which restricts their reinforcing efficiency and dispersion within coating systems. Surface modification with TiO_2 is expected to improve their interfacial compatibility and thermal stability, thereby enhancing the integrity and compactness of the protective char layer formed during combustion [27].

Based on these considerations, an organic–inorganic hybrid intumescent coating was developed by incorporating TiO_2-modified halloysite nanotubes (Ti-HNTs) into a conventional intumescent flame-retardant (IFR) system consisting of waterborne epoxy resin, ammonium polyphosphate (APP), melamine (MEL), pentaerythritol (PER), and boric acid (BA). The hypothesis of this study is that Ti-HNTs can simultaneously act as a physical reinforcing skeleton and a Lewis acid catalyst in the intumescent flame-retardant system, improving interfacial compatibility between inorganic fillers and the organic matrix, promoting the formation of a dense and thermally stable intumescent char layer, and consequently enhancing the fire resistance, smoke suppression, and mechanical integrity of the coating under battery thermal runaway conditions. To verify this hypothesis, Ti-HNTs were synthesized and incorporated into the IFR coating, and the effects of Ti-HNT content and coating thickness on the fire resistance, smoke suppression, thermal insulation, and impact resistance of the coatings were systematically investigated. Furthermore, the synergistic flame-retardant mechanism of Ti-HNTs in the intumescent coating was analyzed through structural characterization and combustion-performance evaluation.

2. Experimental

2.1. Material

The Halloysite nanotubes were purchased from Xi'an Mengchuangda Biotechnology Co., Ltd. (according to their material safety data sheet (MSDS), with outer diameters of 30–70 nm and lengths ranging from 200 to 800 nm, Xi'an, China), anhydrous ethanol from

Tianjin Zhiyuan Chemical Reagent Co., Ltd. (Tianjin, China). Waterborne epoxy resin from Wuxi Honghui New Materials Co., Ltd. (Wuxi, China), and polyphosphoric acid ammonium from Tianjin Zhonglian Chemical Reagent Co., Ltd. (Tianjin, China). Nitric acid, tetraisobutyl titanate, pentaerythritol, melamine, and boric acid were purchased from Guojun Group Chemical Reagent Co., Ltd. (Shanghai, China).

2.2. Preparation of Modified Halloysite

Ethanol and tetrabutyl titanate were mixed in a volume ratio of 10:40 to prepare a solution. While stirring at approximately 1000 rpm, 1 milliliter of concentrated nitric acid was gradually added, and stirring was continued for 5 min. Subsequently, this solution was slowly added drop-by-drop to 100 milliliters of deionized water, and the mixture was continuously stirred in the water for 30 min. Following that, the mixed solution was allowed to stand and age at room temperature for 24 h, resulting in the formation of a sol–gel system consisting of tetrabutyl titanate, ethanol, concentrated nitric acid, and water. Next, the prepared sol–gel system was added to 10 g of pre-prepared halloysite (HNTs) placed in a 200-milliliter beaker, and the mixture was stirred slowly for 1 h. After the reaction had proceeded for 20 h, a high-speed centrifuge was utilized to centrifuge the sample at 9000 rpm for 10 min. Subsequently, the sample was washed once with ethanol and twice with distilled water. Finally, the sample was dried at 100 °C for 5 h, thus obtaining the final product, Ti-HNTs.

2.3. Preparation of Organic–Inorganic Hybrid Expanding Coatings

Prior to spraying, the surface of the aluminum plate (measuring 10 × 10 × 0.3 cm^3) was processed through polishing with 400# sandpaper followed by rinsing with absolute ethanol. The composition of the Ti-HNTs flame-retardant coating is presented in Table 2. Polyphosphoric acid ammonium, melamine, pentaerythritol, borax, and Ti-HNTs were weighed and placed into a beaker. Subsequently, deionized water was added. The mixed slurry was dispersed with a high-speed mechanical stirrer at 800 r/min for 30 min, followed by 15 min ultrasonic treatment at 300 W power to alleviate nanoparticle agglomeration. An automatic film coater with a scraper gap of moving speed of 10 mm/s was adopted to control the coating thickness accurately and guarantee experimental repeatability of parallel samples. After that, waterborne epoxy emulsion and deionized water were added, and mechanical stirring was sustained for an additional 30 min. The coating was applied to the aluminum plate using a coating machine and then cured after being conditioned at a humidity of 75% and a temperature of 40 °C for 72 h.

Table 2. The composition of Ti-HNTs flame-retardant coating.

Component	*TiH-IFR-1* (g)	*TiH-IFR-2* (g)	*TiH-IFR-3* (g)	*TiH-IFR-4* (g)	*TiH-IFR-5* (g)
Ti-HNTs	0	2	4	6	8
APP	28	28	28	28	28
PER	16	16	16	16	16
MEL	16	16	16	16	16
BA	2	2	2	2	2
Waterborne Epoxy Resin	30	30	30	30	30
H_2O	40	38	36	34	32

2.4. Characterization

The Fourier Transform Infrared Spectroscopy (FTIR) test was carried out by the Nicolet 6700 spectrometer (Nicolet Inc., Green Bay, WI, USA).

The thermogravimetric analysis (TGA) and thermogravimetric-infrared (TG-IR) was conducted on the Q5000 thermal analyzer (TA Company, Westlake, OH, USA), with a heating rate of 20 °C/min under nitrogen atmosphere.

The transmission electron microscope (TEM) images were obtained by dropping the sample aqueous solution onto a copper grid and observing it under an accelerating voltage of 20 kV.

The scanning electron microscope (SEM) images were collected by Zeiss Gemini SEM500 (Oberkochen, Germany) at an accelerating voltage of 5 kV.

The X-ray photoelectron spectroscopy (XPS) analysis was performed using the VG ESCALB MK-II spectrometer (VG Scientific, East Grinstead, UK) with Al Kα radiation (1486.6 eV), and all binding energies were calibrated against the adventitious C 1s peak at 284.8 eV.

The fire-resistance test was conducted on a self-built simulated combustion device with a propane blowtorch (nozzle diameter 20 mm, flame core temperature ~1000 °C, surface heat flux ~50 kW/m^2) at a fixed torch-to-sample distance of 10 cm; the 10 × 10 × 0.3 cm aluminum specimen with 100 cm^2 effective exposed area was monitored by a back-center K-type thermocouple and an infrared camera, with each 10 min test repeated three times.

The smoke density test was performed on a Yangyi Wuliu VOUCH 5920 chamber (Suzhou, China) following ASTM E662 in flameless mode (25 kW radiant heat source) with 76 × 76 mm specimens; D4, D10 and Dmax values were recorded, and each sample was tested in triplicate.

The high-temperature impact coupling test was completed at the Testing Center of Huating (Hefei, China) Power using a customized pneumatic bench with synchronous 1000 ± 50 °C flame scouring; a 0.5 MPa impact load was applied to the center of 10 × 10 cm samples (impact head diameter 30 mm) within 30 s, with each test repeated three times.

3. Results and Discussion

3.1. Characterization of HNTs and Ti-HNTs

The thermal behavior of HNTs and Ti-HNTs blends within the temperature range from room temperature to 800 °C was examined using TGA and DTG, as depicted in Figure 1a,b. From the Ti-HNTs data in Figure 1a, an enhanced mass change is observable in the 200–300 °C range. This could be attributed to the desorption of adsorbed water molecules [28] and the structural dehydroxylation of Al-OH groups within the structure between 450 and 550 °C [29]. The enhanced mass change in Ti-HNTs at 200–300 °C in Figure 1a underscores the successful incorporation of TiO_2 into the HNTs cavities. Overall, the thermal stability of Ti-HNTs was found to be superior to that of unmodified HNTs. In Table 3, the temperature corresponding to a 5% mass loss ($T_{-5\%}$) of Ti-HNTs was lower (415.4 °C), indicating that the modified material begins to decompose at a lower temperature. However, as the temperature rises, the performance of Ti-HNTs at $T_{-10\%}$ and T_{max} temperatures demonstrates greater heat resistance. These temperatures increased to 499.6 °C and 500.3 °C, respectively, which are significantly higher than those of unmodified HNTs at $T_{-10\%}$ (488.5 °C) and T_{max} (491.2 °C). Consequently, Ti-HNTs have proven to be more stable in high-temperature environments, and their enhanced ability to withstand higher temperatures has been confirmed. This property confers a distinct advantage in high-temperature applications, suggesting that as a modified material, it has the potential to offer better performance and a longer service life under high-temperature conditions.

To verify the successful preparation of Ti-HNTs, their chemical structure and elemental composition were analyzed via FTIR and XPS. As depicted in Figure 1b, the two characteristic spectral bands of HNTs at 3692 and 3622 cm^{-1} stem from the telescopic vibration of Al-OH groups on the HNTs' surface. Additionally, the Al-O-Si deformation and the O-H deformation of the internal hydroxyl groups are manifested as peaks at 541 and 916 cm^{-1}, respectively [30]. The peak near 1000 cm^{-1} is ascribed to the Si-O group in HNTs. All these peaks were also present in the FTIR spectra of Ti-HNTs [31]. As illustrated in Figure 1d, XPS spectra were utilized to further explore the surface elemental composition of Ti-HNTs. The results revealed the presence of Ti, O, C, N, Si, and Al in the samples, thereby confirming the chemical composition of Ti-HNTs. Here, Si and Al were predominantly derived from the HNTs carriers. As shown in Figure 1e, after the deconvolution of C1s, three overlapping peaks can be obtained. The peaks at 284.8 eV, 286.8 eV, and 288.6 eV can be respectively fitted to the C-C band, the C-O-C band, and the O-C = O band [32]. As presented in Figure 1f, the peaks at 458.7 eV and 464.4 eV are attributed to Ti2p3/2 and Ti2p1/2 of $Ti4^{+}$ in TiO_2 [33]. The XPS results indicate that the composites are composed of TiO_2 and HNTs.

The microstructures of HNTs before and after modification were characterized using transmission electron microscopy (TEM). As depicted in Figure 2a–c [34], the hollow tubular structures of HNTs, with diameters ranging from 50 to 70 nm and lengths from 0.5 to 2 μm, were clearly visible. In Figure 2d–f, it can be observed that TiO_2 nanoparticles are randomly deposited on the surface of HNTs. The particle size of these TiO_2 nanoparticles was determined to be in the range of 10–80 nm. The presence of TiO_2 nanoparticles on the surface of HNTs confirms the successful loading of TiO_2 onto HNTs.

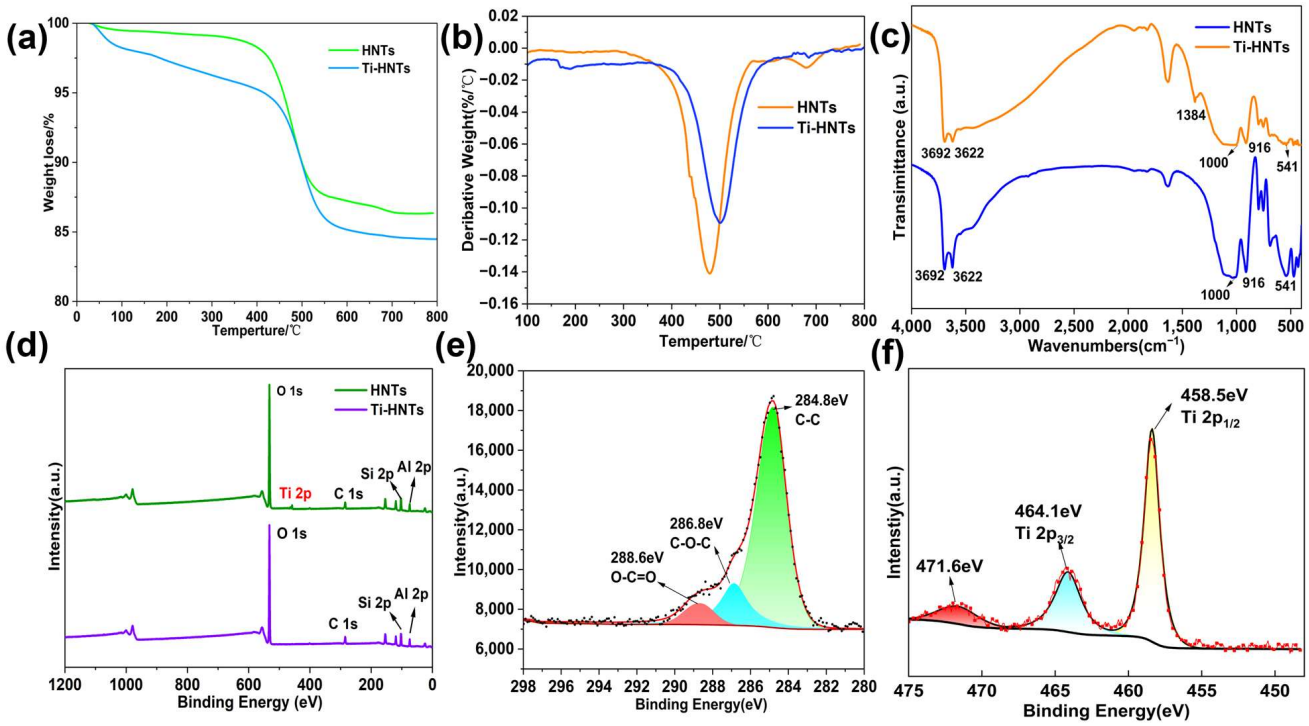


Figure 1. (**a**) TGA diagram of HNTs and Ti-HNTs, (**b**) DTG diagram of HNTs and Ti-HNTs, (**c**) FTIR diagram of HNTs and Ti-HNTs, (**d**) XPS diagram of HNTs and Ti-HNTs, (**e**) C1s peak diagram of Ti-HNTs, (**f**) Ti2p peak diagram of Ti-HNTs.

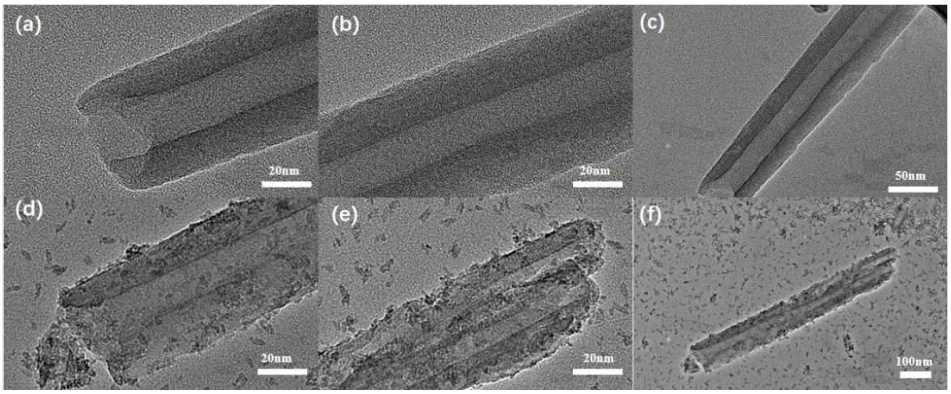


Figure 2. (**a**–**c**) TEM images of HNTs, (**d**–**f**) TEM images of Ti-HNTs.

Table 3. TGA data of HNTs before and after modification.

Sample	$T_{-5\%}$ (°C)	$T_{-10\%}$ (°C)	T_{max} (°C)	*Residue at 800* °C (%)
HNTs	458.2	488.5	491.2	86
Ti-HNTs	415.4	499.6	500.3	84

3.2. Screening and Optimization of Coatings

3.2.1. Screening Emulsions

The experimental results presented in Table 4 show that the waterborne epoxy resin emulsion exhibited the highest expansion ratio (7.1) among the four investigated emulsion systems, indicating its superior ability to form an effective thermally insulating char layer during combustion. Compared with pure acrylic, silicone-acrylic, and vinyl acetate-acrylate emulsions, the epoxy-based system generated a more compact and stable expanded char, resulting in enhanced thermal insulation performance. This behavior is consistent with previous studies showing that the cross-linked epoxy network plays a crucial role in promoting the formation of a continuous and mechanically stable char layer during thermal decomposition, thereby improving the fire-protection efficiency of intumescent coatings [35,36]. Furthermore, the APP/MEL/PER intumescent system cooperates with the epoxy matrix to promote char formation and suppress heat and mass transfer during combustion [37]. Compared with previously reported waterborne epoxy intumescent coatings reinforced with inorganic fillers, the Ti-HNTs incorporated in this work are expected to further improve the integrity of the expanded char by enhancing the compatibility between the inorganic phase and the epoxy matrix, thereby forming a denser and more stable thermal barrier during fire exposure [38]. Therefore, the superior expansion performance observed in the present study can be attributed not only to the intrinsic characteristics of the cross-linked epoxy matrix but also to the synergistic reinforcement provided by Ti-HNTs.

Table 4. Emulsion formulations of different substrates and their coating expansion rates after refractory experiment emulsions.

	Matrix Emulsion (g)	*APP* (g)	*MEL* (g)	*PER* (g)	*Expansion Rate* (Times)
Pure acrylic	30	28	16	16	3.5
Silicone-acrylic	30	28	16	16	4.0
Vinyl acetate-acrylate	30	28	16	16	5.5
Waterborne epoxy Resin	30	28	16	16	7.1

3.2.2. Screening of Coating Formula Ratio and Thickness

The addition ratios of Ti-HNTs can alter the intumescence, thermal stability, and fire resistance of the coatings. As the proportion of Ti-HNTs rises, it exerts varying enhancement effects within the coating, improving both its heat-shielding capabilities and intumescence. Additionally, coating thickness is a crucial factor influencing fire resistance; thicker coatings generally offer better fire protection, yet they also increase material cost and weight. Consequently, orthogonal experiments were designed to systematically evaluate the performance of coatings with different combinations of Ti-HNTs ratios and thicknesses, ultimately determining the optimal formulation. In this study, orthogonal experiments (presented in Table 5) were devised to comprehensively investigate how different Ti-HNTs ratios and coating thicknesses impact coating properties.

Five distinct Ti-HNTs addition ratios (0%, 2%, 4%, 6%, and 8%) were selected for the experiments and paired with three different coating thicknesses. The design thicknesses were 0.5 mm, 1 mm, and 1.5 mm, with the actual thicknesses after curing being 0.31 mm, 0.65 mm, and 0.92 mm, labeled as thicknesses 1, 2, and 3 in the table respectively. Coatings with different thickness-ratio combinations were named as (TiH-IFR-1-1, TiH-IFR-1-2, etc.). From the results in Table 5 for thickness 3, it is evident that without the addition of Ti-HNTs, the organic portion of the coating exhibits a relatively good swelling effect. However, as Ti-HNTs are added, the swelling effect first increases and then decreases. Specifically, at a 4% Ti-HNTs addition, the swelling effect surpasses that of the pure inorganic coating. These findings suggest that the TiH-IFR-3-2 coating represents the optimal formulation for achieving the best intumescent effect. Through this experimental design, the objective was to evaluate the combined influence of different Ti-HNTs proportions and coating thickness on fire performance.

Table 5. Coating expansion rates with different Ti-HNTs dosage and different thicknesses.

Sample ID	Ti-HNTs Content (wt%)	Designed Thickness (mm)	Actual Cured Thickness (mm)
TiH-IFR-1-1	0	0.5	0.31
TiH-IFR-1-2	0	1	0.65
TiH-IFR-1-3	0	1.5	0.92
TiH-IFR-2-1	2	0.5	0.31
TiH-IFR-2-2	2	1	0.65
TiH-IFR-2-3	2	1.5	0.92
TiH-IFR-3-1	4	0.5	0.31
TiH-IFR-3-2	4	1	0.65
TiH-IFR-3-3	4	1.5	0.92
TiH-IFR-4-1	6	0.5	0.31
TiH-IFR-4-2	6	1	0.65
TiH-IFR-4-3	6	1.5	0.92
TiH-IFR-5-1	8	0.5	0.31
TiH-IFR-5-2	8	1	0.65
TiH-IFR-5-3	8	1.5	0.92

3.3. Analysis of Coatings

The surface morphology of the coatings was observed via scanning electron microscopy (SEM). As depicted in Figure 3a, the coated surfaces, at different Ti-HNTs ratios and coating thicknesses, exhibited good flatness and densification. Notably, when 4%

Ti-HNTs were added and the coating thickness was 1.5 mm, the coating surface presented the best uniformity and Ti-HNTs dispersion effect. As shown in Figure 3b, under these conditions, the Ti-HNTs were evenly distributed within the aqueous epoxy resin matrix. No obvious agglomeration or deposition phenomena were observed, and the Ti-HNTs were embedded in the coating in a more homogeneous fashion.

It is worth noting that although the designed coating thickness was 1.5 mm, the final cured thickness was 1.1 mm. This indicates that a certain degree of shrinkage occurred during the curing process. Nevertheless, the cured thickness was still sufficient to meet the fire-resistance requirements. The coating surface was smooth and dense, with no appearance of defects such as cracks or pores. This suggests that the coating structure was stabilized under this formulation and thickness, and the addition of Ti-HNTs effectively enhanced the overall performance of the coating.

However, as can be seen in Figure 4a,g,j,m, at a coating thickness of 0.5 mm, the Ti-HNTs showed poor dispersion. Due to the thin coating, the Ti-HNTs were not uniformly distributed in the substrate, and minor aggregation or deposition of Ti-HNTs occurred in some areas. This non-uniform distribution might lead to a compromise in the overall performance of the coating, particularly in terms of fire performance and thermal stability. Thinner coatings may not enable the full utilization of the enhancing effect of Ti-HNTs, thereby affecting the intumescence effect and heat-shielding properties of the coatings.

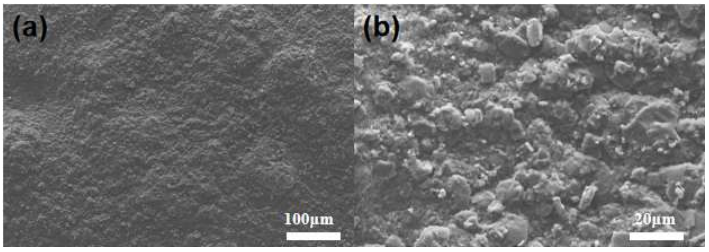


Figure 3. Surface SEM images of the cured TiH-IFR-3-2 intumescent coating: (**a**) overall surface morphology and compactness at low magnification; (**b**) dispersion state of Ti-HNTs in the waterborne epoxy matrix at high magnification.

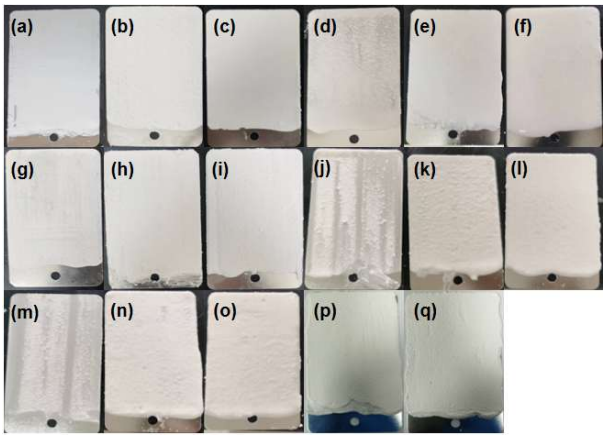


Figure 4. Post-combustion char SEM micrographs: (**a**–**c**) TiH-IFR-1 (1.0/1.5/2.0 mm), (**d**–**f**) TiH-IFR-2 (1.0/1.5/2.0 mm), (**g**–**i**) TiH-IFR-3 (1.0/1.5/2.0 mm), (**j**–**l**) TiH-IFR-4 (1.0/1.5/2.0 mm), (**m**–**o**) TiH-IFR-5 (1.0/1.5/2.0 mm), (**p**,**q**) pure HNTs coating (1.0 mm, 1.5 mm).

3.4. Fire-Resistance Analysis

3.4.1. Fire-Resistance Test

To evaluate the impact of different Ti-HNTs ratios and coating thicknesses on the fire resistance of fire-resistant coatings, a home-made simulated combustion method device

was utilized in this study to conduct fire-resistance tests. A simple schematic diagram of the device is presented in Figure 5a. The simulated combustion test aimed to mimic the thermal exposure of the new-energy vehicle battery system in a high-temperature environment, thereby testing the performance of coatings with different formulations at high temperatures, with a primary focus on evaluating the back temperatures of the coatings.

Firstly, as depicted in Figure 5b, the fire resistance of the pure plate and three coatings, namely TiH-IFR-3 and TiH-IFR-5, was compared. In the control (TiH-IFR-1-2) coatings, after 10 min of fire-resistance testing (where all temperatures mentioned hereinafter refer to the back temperatures of the aluminum plates at the 10 min mark of the fire-resistance experiments), the back temperature of the aluminum plate reached 426.5 °C, indicating poor fire-resistance performance. In contrast, for the TiH-IFR-3-2 coating, the back temperature of the aluminum plate was 202.1 °C, demonstrating a significant improvement in the coating's fire resistance, as this temperature was significantly lower than that of the control. When the proportion of Ti-HNTs was increased further to 8%, the maximum temperature of the coating rose to 321.5 °C. Although this temperature was still lower than that of the TiH-IFR-1-2 coatings, the high proportion of Ti-HNTs might have led to an overly dense coating structure. This, in turn, affected the coating's expansion and thermal isolation capabilities, resulting in a slight decline in its refractory properties. Consequently, the TiH-IFR-3-2 coating is regarded as the optimal choice in terms of fire resistance.

This study also delved deeply into the effect of different coating thicknesses on fire resistance. Three coatings, TiH-IFR-3-1, TiH-IFR-3-2, and TiH-IFR-3-3, were selected for testing. As shown in Figure 5c, the TiH-IFR-3-1 coating had a maximum temperature of 254.2 °C. While it provided a certain level of fire resistance, the thinness of the coating meant it could not offer adequate thermal isolation. The TiH-IFR-3-2 coating emerged as the top-performer in terms of fire resistance, with a maximum temperature of 215.9 °C, which was significantly lower than that of the TiH-IFR-3-1 and TiH-IFR-3-3 coatings. This indicates that the TiH-IFR-3-2 coating effectively enhanced the heat-shielding effect and provided better protection for the object in high-temperature environments. Regarding the TiH-IFR-3-3 coating, although it also exhibited good fire resistance, its temperature was slightly higher compared to the TiH-IFR-3-2 coating. This could be attributed to the fact that the overly thick coating affected its flexibility and thermal expansion to a certain extent. In conclusion, the TiH-IFR-3-2 coating was determined to be the best-performing in the fire-resistance test, presenting a thermal-insulation effect of 49.4%. As can be gleaned from the data in Table 3 for this percentage-thickness formulation, the expansion effect was also optimal, offering effective thermal-isolation protection for the object.

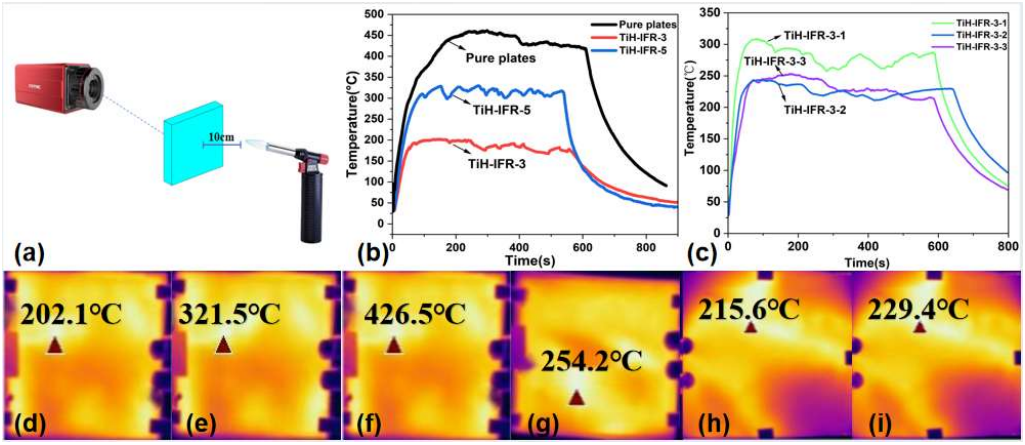


Figure 5. (**a**) Schematic diagram of simulated combustion test, (**b**) pure plate, TiH-IFR-3/5 coating combustion back-temperature profiles, (**c**) TiH-IFR-3-1/2/3/coating combustion back-temperature

profiles, (**d**–**f**) pure plate, TiH-IFR-3/5 coating fire-resistant experimental infrared images, (**g**–**i**) TiH-IFR-3-1/2/3 coating fire-resistance experiment infrared images.

3.4.2. Analysis of the Carbon Layer

Following the refractory performance tests, the digital photographs of the charcoal layers are presented in Figure 6. As depicted in Figure 6i, the 1.5 mm coated carbon layer of TiH-IFR-3-2 exhibits the optimal swelling effect. Similarly, as shown in Figure 6r, the pure HNTs carbon layer also demonstrates a relatively good swelling effect. However, during the test, the carbon layer showed poor stability and some mobility during its formation process.

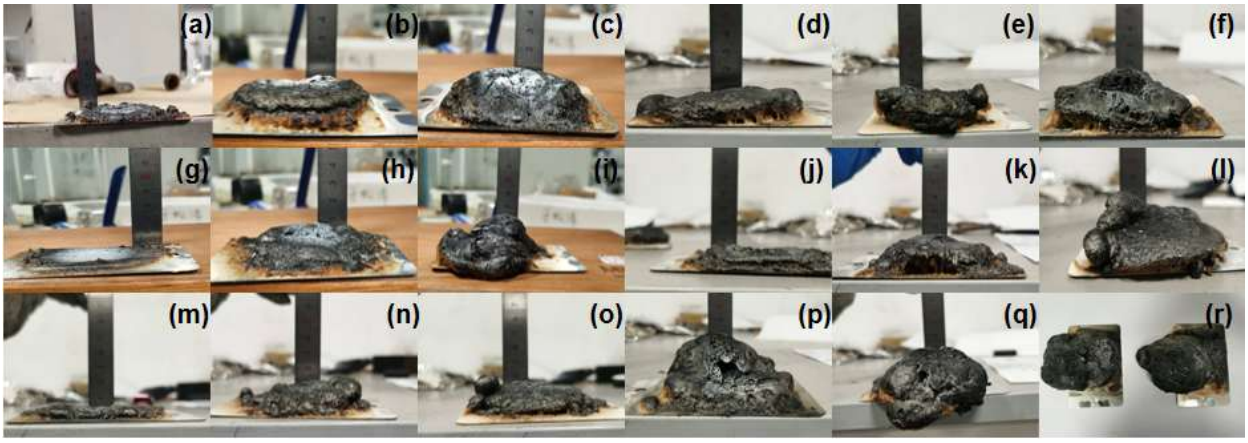


Figure 6. (**a**–**c**) TiH-IFR-1-1/2/3 carbon layer, (**d**–**f**) TiH-IFR-2-1/2/3 carbon layer, (**g**–**i**) TiH-IFR-3-1/2/3 carbon layer, (**j**–**l**) TiH-IFR-4-1/2/3 carbon layer, (**m**–**o**) TiH-IFR-5-1/2/3 carbon layer, (**p**,**q**) coated carbon layer with a design thickness of 1.0, 1.5 mm for pure HNTs, (**r**) top view of a carbon layer coated with pure HNTs.

In this study, scanning electron microscopy (SEM) was employed to analyze the outer and inner surfaces of the coated carbon layer, thereby further exploring the role of Ti-HNTs in the coating, particularly its influence on the formation process of the carbon layer. Regarding the analysis of the outer surface, the uniformity and denseness of the outer surface of the carbon layer formed by the coating can be observed from the (a) and (b) images in SEM Figure 7. The structure of the outer surface of the charcoal layer is relatively flat, with fine particles arranged regularly. Cracks and obvious pores are scarcely present on the surface. This suggests that the coating possesses good thermal-isolation properties at high temperatures, effectively preventing the spread of flame and heat.

When analyzing the inner surface, with the aid of SEM Figure 7c,d, the inner surface of the carbon layer was examined. It was found that the inner surface of the carbon layer displayed an obvious honeycomb-bubble structure, indicating a good expansion effect and a more homogeneous structure. Honeycomb bubbles are the typical structure resulting from the expansion of the carbon layer under high-temperature conditions. They can effectively isolate heat propagation, reducing the heat transfer to the substrate. The relatively uniform distribution of the bubbles implies that the coating undergoes a good expansion reaction at high temperatures, forming a stable and dense thermal-insulation layer. This uniform honeycomb structure contributes to the coating's thermal isolation and fire-resistance capabilities.

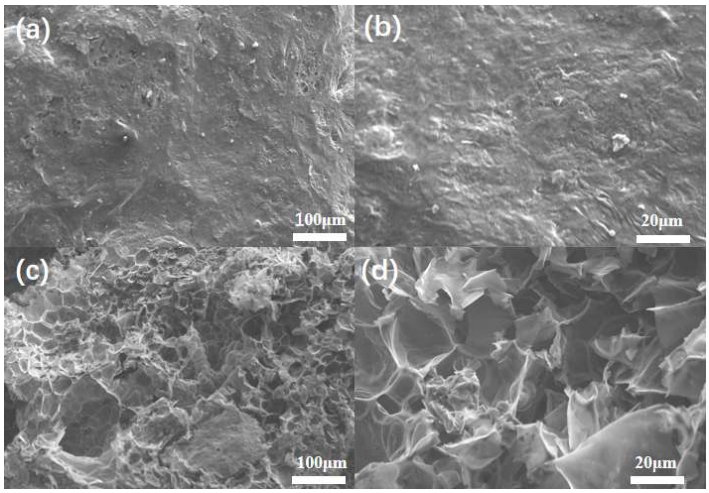


Figure 7. (**a**,**b**) SEM image of the outer surface of the TiH-IFR-3-2 carbon layer, (**c**,**d**) SEM image of the inner surface coating of the TiH-IFR-3-2 carbon layer.

3.4.3. Smoke Density Test

In the event of a fire, the escape of personnel can be threatened by toxic substances and smoke [39]. To investigate the smoke-suppression performance of the coating, a smoke-density test was conducted under the condition of a 25 kW flameless test. The comparison of the light-density curves is presented in Figure 8 and Table 6.

During the smoke-density test, TiH-IFR-3-2 exhibited better performance advantages. It had a lower smoke density (Dmax = 22.55, which was significantly lower than 24.67 of TiH-IFR-2/4-2), a more gradual trend of smoke generation (D4 = 22.29, D10 = 21.02, indicating a stable state of medium-term smoke), and better combustion stability (with a quality-loss rate of 2.64%, determined to be the lowest among the five groups).

The time when the smoke density reached the critical threshold (Ds = 16) was the same as that of TiH-IFR-1/5-2 (91 s). However, the time of smoke-peak occurrence (293 s) was later than that of TiH-IFR-2/4-2 (316 s). This indicates that the combustion process could be more effectively controlled, and the accumulation of smoke concentration could be effectively delayed. When comprehensively considering the amount, rate, and combustion-decomposition characteristics of smoke generation, it was confirmed that TiH-IFR-3-2 was significantly superior to other groups in terms of safety, visibility maintenance, and fire-resistance performance. Thus, it was determined as the preferred solution for low-smoke and high-stability scenarios.

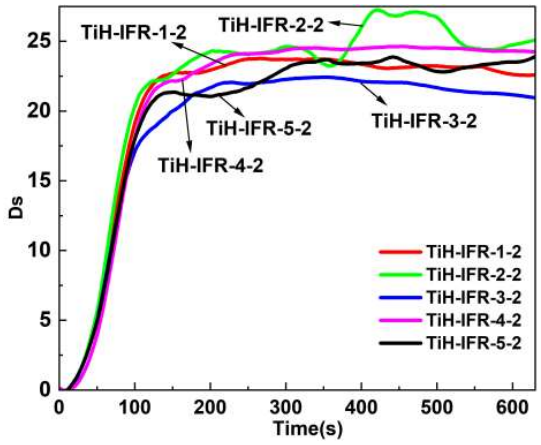


Figure 8. Specific optical density curves of TiH-IFR-1/2/3/4/5-2 coatings.

Table 6. Detailed values for smoke density tests.

Sample	D_4	D_{10}	D_{max}
TiH-IFR-1-2	23.83	21.84	24.33
TiH-IFR-2-2	24.11	24.84	27.83
TiH-IFR-3-2	22.29	21.02	22.55
TiH-IFR-4-2	24.16	24.16	24.66
TiH-IFR-5-2	21.60	23.57	29.59

3.5. Analysis of TG-IR

Based on the thermogravimetric-infrared analysis (TG-IR) curve in Figure 9, several characteristic peaks are observable. Specifically, a peak at 2358 cm^{-1} is attributed to CO_2. At 700 °C, another peak at 2180 cm^{-1} is assigned to CO [40]. A peak at 1744 cm^{-1} is attributed to the presence of C = O [41]; the peak at 1279 cm^{-1} stems from the vibration of C-O-C within the epoxy resin moiety [42], and the peak at 680 cm^{-1} is attributed to the vibration of Si-O in the Ti-HNTs [43]. From these analyses, it is evident that during pyrolysis, the degradation of functional groups such as C-O-C and C = O coincides with the coating's degradation, accompanied by the release of gases like CO_2 and CO. Notably, the release of CO was effectively suppressed, with only a small amount generated around 700 °C. The Ti-O-C and C = O functional groups were also released during this process. Importantly, the Si-O structure of Ti-HNTs remained stable. This property likely contributes positively to the material's thermal stability and flame retardancy. For instance, the stabilized Si-O structure may enhance the coating's overall structural integrity, rendering it more resistant to decomposition at high temperatures, thereby improving thermal stability. Simultaneously, this stability may influence the gas-release process and the coating's flame-retardant mechanism, potentially enhancing its flame-retardant performance.

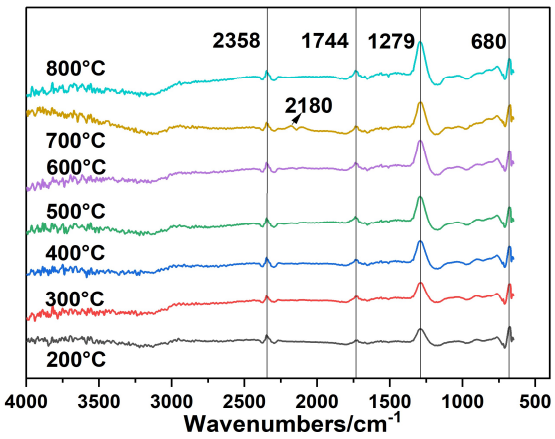


Figure 9. TG-IR of TiH-IFR-3-1-2.

3.6. High-Temperature Impact Coupling Test

In the practical application scenarios of battery thermal runaway protection coatings, the coatings need to withstand the dual effects of high-temperature flames and mechanical impacts simultaneously. To this end, a high-temperature impact coupling test was designed in this study to simulate the challenges to the coating's structural integrity caused by the sudden increase in internal pressure during the thermal runaway of power batteries. TiH-IFR-3-2 coating was selected for coupled high-temperature impact characterization for the following reasons: among all gradient Ti-HNTs doping groups, TiH-IFR-3 series exhibited balanced char-forming efficiency and smoke suppression performance, and the 1.5 mm thickness sample achieved the optimal comprehensive thermal insulation effect in the

preliminary gradient thickness test, which can best reflect the synergistic flame-retardant mechanism of Ti-HNTs modified intumescent coating.

The testing device utilized a customized pneumatic blast furnace (Figure 10a), which could achieve a synergistic effect of 0.5 MPa impact loading and 1000 °C flame spraying within 30 s. In the experiment, the optimized formula TiH-IFR-3-2 coating (with a thickness of 1.5 mm) was selected, and the uncoated aluminum alloy plate was used as the control group.

After the impact, it was observed that on the back of the experimental group's plate (Figure 10b), only a shallow indentation with a diameter of approximately 30 mm was formed, without cracks or penetrative damage. In contrast, for the control group (the right side of Figure 10c), the uncoated plate underwent severe plastic deformation under the impact. A penetrative breach with a diameter of 25 mm appeared in the central area, and the metal at the edges was torn and turned outwards. Obvious high-temperature burning marks could be seen on the back.

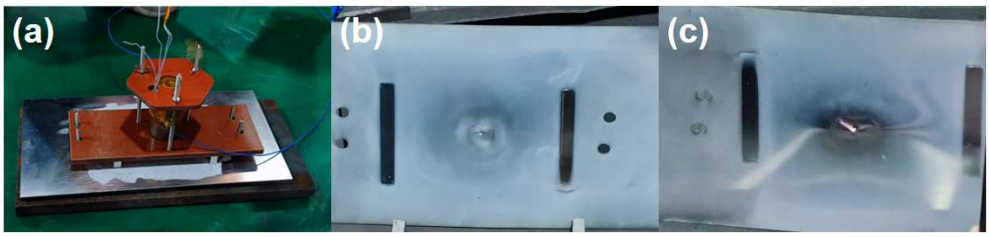


Figure 10. (**a**) The device for high-temperature impact coupling test. (**b**) The photo of the back of the plate after the test in the TiH-IFR-3-2 experimental group. (**c**) The photo of the back of the plate after the test in the control group.

4. Conclusions

All performance evaluations in this work were designed based on the typical thermal runaway scenarios of power batteries. The test results can effectively characterize the fire protection effect of the coating on battery systems, providing data support for subsequent practical battery module verification. In this study, organic–inorganic composite intumescent fireproofing coatings based on modified halloysite (Ti-HNTs) were successfully synthesized. A comprehensive array of characterization techniques, including XPS, FTIR, TEM, and SEM, were employed to thoroughly validate the impact of Ti-HNTs modification. The XPS and FTIR analysis results indicated that the chemical modification of the Ti-HNTs surface was successfully achieved. This led to a significant enhancement in its compatibility with the substrate material. Moreover, TEM images clearly demonstrated the successful loading of TiO_2 onto the inner and outer surfaces of the hollow-structured HNT. During the coating substrate screening experiments, various aqueous emulsions were investigated comparatively. The results identified aqueous epoxy resin emulsion as the most suitable substrate material, owing to its outstanding adhesion and heat-resistant properties. Through a systematic examination of coating performance under different combinations of Ti-HNTs ratios and coating thicknesses, the TiH-IFR-3-2 coating was found to exhibit excellent fire-resistance. Fire-resistance test data revealed that its thermal-insulation effect reached as high as 49.4%, its expansion multiplier attained 37.7, the back-temperature of the aluminum plate was significantly lower than that of other coatings, and its fire-resistance effect was markedly superior to coatings with other ratios and thicknesses. Upon analyzing the coating's charcoal layer using SEM, it was discovered that the coating could form a uniform and dense charcoal layer at high temperatures. The inner surface presented a honeycomb-bubble structure, which significantly enhanced the coating's thermal-isolation ability and stability. This structure effectively prevented heat transfer after expansion, further augmenting the fire-resistance. The smoke-density test results indicated that the

TiH-IFR-3-2 coating had a low smoke density (Dmax = 22.55), a gradual smoke-generation trend, and good combustion stability (with a mass-loss rate of merely 2.64%). In additional impact resistance tests, the coating demonstrated exceptional structural integrity by withstanding a simulated battery pressure relief impact of 0.5 MPa without any signs of penetration. Even under such extreme mechanical stress, the coating maintained its thermal barrier function, ensuring consistent heat insulation performance.

These results further validate the coating's reliability in real-world scenarios, where it must simultaneously resist both high-temperature fire and sudden mechanical shocks during battery thermal runaway events. These features contributed to its outstanding performance in terms of safety and visibility maintenance. In conclusion, the organic–inorganic composite intumescent fireproof coating developed in this study showcases excellent fire resistance, an outstanding thermal-isolation effect, and good smoke-suppression performance. It can effectively and efficiently enhance the fire-proof capability of the battery system, thus holding great promise for broad applications in the field of new-energy vehicle batteries.

Author Contributions: Conceptualization, Y.X. and W.X.; methodology, Y.X. and W.W.; software, Y.X.; validation, Y.X., L.Q. and W.W.; formal analysis, Y.X.; investigation, Y.X. and L.Q.; resources, Y.H.; data curation, Y.X. and W.W.; writing—original draft preparation, Y.X.; writing—review and editing, W.X. and Y.H.; visualization, L.Q.; supervision, W.X. and Y.H.; project administration, W.X.; funding acquisition, Y.H. All authors have read and agreed to the published version of the manuscript.

Funding: This work was financially supported by the Key Research and Development Program of Anhui Province (Grant No. 2023z04020017, *Research and Development of Battery System without Thermal Uncontrolled Failure Based on High Insulation and High Expansion Fireproof Coatings*), the Innovation Research Group Project of the National Natural Science Foundation of China (Grant No. 52321003, *Fire Combustion Dynamics*), and the Education Department Fund of Anhui Province (Grant No. 2022AH050253).

Data Availability Statement: The data that support the findings of this study are available from the corresponding author upon reasonable request.

Acknowledgments: We are grateful for the financial support from the Key Research and Development Program of Anhui Province, "Research and Development of Battery System without Thermal Uncontrolled Failure Based on High Insulation and High Expansion Fireproof Coatings (2023z04020017)", and the Innovation Research Group Project of the National Natural Science Foundation of China, "Fire Combustion Dynamics" (52321003); we are also grateful for the financial support from the Education Department Fund of Anhui Province (2022AH050253).

Conflicts of Interest: The authors declare no conflict of interest.

References

1. Yuan, L.; Dubaniewicz, T.; Zlochower, I.; Thomas, R.; Rayyan, N. Experimental study on thermal runaway and vented gases of lithium-ion cells. *Process Saf. Environ. Prot.* **2020**, *144*, 186–192. [CrossRef]
2. Wang, Q.; Mao, B.; Stoliarov, S.I.; Sun, J. A review of lithium ion battery failure mechanisms and fire prevention strategies. *Prog. Energy Combust. Sci.* **2019**, *73*, 95–131. [CrossRef]
3. Zhao, L.; Hou, J.; Feng, X.; Xu, J.; Xu, C.; Wang, H.; Liu, H.; Hou, B.; Rui, X.; Gu, Y.; et al. The trade-off characteristic between battery thermal runaway and combustion. *Energy Storage Mater.* **2024**, *69*, 103380. [CrossRef]
4. Hu, D.; Huang, S.; Wen, Z.; Gu, X.; Lu, J. A review on thermal runaway warning technology for lithium-ion batteries. *Renew. Sustain. Energy Rev.* **2024**, *206*, 114882. [CrossRef]
5. Wu, X.; Mo, C.; Xie, J.; Xu, Y.; Li, Y.; Chen, H. Experimental study of a novel strategy to construct the battery thermal management module by using tubular phase change material units. *J. Energy Storage* **2021**, *39*, 102585. [CrossRef]
6. Zhang, J.; Li, X.; Wang, Z.; Guo, H.; Yan, J. Experimental and numerical studies on an efficient transient heat transfer model for air-cooled battery thermal management systems. *J. Power Sources* **2021**, *490*, 229539. [CrossRef]
7. Feng, X.; Ouyang, M.; Liu, X.; Lu, L.; Xia, Y.; He, X. Thermal runaway mechanism of lithium ion battery for electric vehicles: A review. *Energy Storage Mater.* **2018**, *10*, 246–267. [CrossRef]

8. Wang, K.; Zhang, X.; Li, S.; Chen, M.; Zhao, L.; Liu, J.; Wang, Q. Early warning method and fire extinguishing technology of lithium-ion battery thermal runaway: A review. *Energies* **2023**, *16*, 2960. [CrossRef]
9. Qi, C.; Wang, Y.; Zhang, X.; Li, H.; Chen, M.; Liu, J.; Zhao, L. Study on the thermal runaway characteristics and debris of lithium-ion batteries under overheating, overcharge, and extrusion. *J. Energy Storage* **2023**, *72*, 108821. [CrossRef]
10. International Energy Agency (IEA). *Global EV Outlook 2025*; International Energy Agency: Paris, France, 2025.
11. Jiang, J.; Wang, Q.; Zhang, Y.; Li, S.; Chen, M.; Liu, J.; Zhao, L. Recent advances in passive thermal management for lithium-ion batteries. *Renew. Sustain. Energy Rev.* **2023**, *180*, 113304.
12. International Energy Agency (IEA). *The State of Energy Innovation 2025*; International Energy Agency: Paris, France, 2025.
13. Li, Y.; Zhang, X.; Wang, Q.; Chen, M.; Liu, J.; Huang, P.; Zhao, L. Experimental investigation on thermal management system with flame retardant flexible phase change material for retired battery module. *Appl. Energy* **2022**, *327*, 120109. [CrossRef]
14. Li, S.; Wang, Y.; Chen, M.; Zhang, X.; Liu, J.; Zhao, L. Flexible phase change materials obtained from a simple solvent-evaporation method for battery thermal management. *J. Energy Storage* **2021**, *44*, 103447. [CrossRef]
15. Patel, J.R.; Rathod, M.K. Recent developments in the passive and hybrid thermal management techniques of lithium-ion batteries. *J. Power Sources* **2020**, *480*, 228820. [CrossRef]
16. Sun, J.; Mao, B.; Wang, Q. Progress on the research of fire behavior and fire protection of lithium ion battery. *Fire Saf. J.* **2021**, *120*, 103119. [CrossRef]
17. Wang, Y.-W.; Huang, C.-Y. Thermal explosion energy evaluated by thermokinetic analysis for series- and parallel-circuit NMC lithium battery modules. *Process Saf. Environ. Prot.* **2020**, *142*, 295–307. [CrossRef]
18. Diaz, L.B.; He, X.; Hu, Z.; Restuccia, F.; Marinescu, M.; Barreras, J.V.; Patel, Y.; Offer, G.; Rein, G. Meta-review of fire safety of lithium-ion batteries: Industry challenges and research contributions. *J. Electrochem. Soc.* **2020**, *167*, 090559. [CrossRef]
19. Hou, J.; Wang, L.; Feng, X.; Terada, J.; Lu, L.; Yamazaki, S.; Su, A.; Kuwajima, Y.; Chen, Y.; Hidaka, T.; et al. Thermal runaway of lithium-ion batteries employing flame-retardant fluorinated electrolytes. *Energy Environ. Mater.* **2023**, *6*, e12297. [CrossRef]
20. Dai, X.; Kong, D.; Du, J.; Zhang, Y.; Ping, P. Investigation on effect of phase change material on the thermal runaway of lithium-ion battery and exploration of flame retardancy improvement. *Process Saf. Environ. Prot.* **2022**, *159*, 232–242. [CrossRef]
21. Huang, Q.; Li, X.; Zhang, G.; Weng, J.; Wang, Y.; Deng, J. Innovative thermal management and thermal runaway suppression for battery module with flame retardant flexible composite phase change material. *J. Clean. Prod.* **2022**, *330*, 129718. [CrossRef]
22. Cui, M.; Li, J.; Qin, D.; Sun, J.; Chen, Y.; Xiang, J.; Yan, J.; Fan, H. Intumescent flame retardant behavior of triazine group and ammonium polyphosphate in waterborne polyurethane. *Polym. Degrad. Stab.* **2021**, *183*, 109439. [CrossRef]
23. Tong, C.; Zhang, S.; Zhong, T.; Fang, Z.; Liu, H. Highly fibrillated and intrinsically flame-retardant nanofibrillated cellulose for transparent mineral filler-free fire-protective coatings. *Chem. Eng. J.* **2021**, *419*, 129440. [CrossRef]
24. Delaporte, N.; Perea, A.; Paolella, A.; Dubé, J.; Vigeant, M.-J.; Demers, H.; Clément, D.; Zhu, W.; Gariépy, V.; Zaghib, K. Alumina-flame retardant separators toward safe high voltage Li-Ion batteries. *J. Power Sources* **2021**, *506*, 230189. [CrossRef]
25. Weng, J.; Ouyang, D.; Yang, X.; Chen, M.; Zhang, G.; Wang, J. Alleviation of thermal runaway propagation in thermal management modules using aerogel felt coupled with flame-retarded phase change material. *Energy Convers. Manag.* **2019**, *200*, 112071. [CrossRef]
26. Du, M.; Guo, B.; Jia, D. Newly emerging applications of halloysite nanotubes: A review. *Polym. Int.* **2010**, *59*, 574–582. [CrossRef]
27. Zhang, Y.; Tang, A.; Yang, H.; Ouyang, J. Applications and interfaces of halloysite nanocomposites. *Appl. Clay Sci.* **2016**, *119*, 8–17. [CrossRef]
28. Yao, W.; Zhang, B.; Huang, C.; Ma, C.; Song, X.; Xu, Q. Synthesis and characterization of high efficiency and stable Ag_3PO_4/TiO_2 visible light photocatalyst for the degradation of methylene blue and rhodamine B solutions. *J. Mater. Chem.* **2012**, *22*, 4050–4055. [CrossRef]
29. Chen, Y.; Zhang, Y.; Liu, J.; Zhang, H.; Wang, K. Preparation and antibacterial property of polyethersulfone ultrafiltration hybrid membrane containing halloysite nanotubes loaded with copper ions. *Chem. Eng. J.* **2012**, *210*, 298–308. [CrossRef]
30. Yuan, P.; Southon, P.D.; Liu, Z.; Green, M.E.R.; Hook, J.M.; Antill, S.J.; Kepert, C.J. Functionalization of Halloysite Clay Nanotubes by Grafting with γ-Aminopropyltriethoxysilane. *J. Phys. Chem. C* **2008**, *112*, 15742–15751. [CrossRef]
31. Mishra, G.; Mukhopadhyay, M. TiO_2 decorated functionalized halloysite nanotubes (TiO_2@HNTs) and photocatalytic PVC membranes synthesis, characterization and its application in water treatment. *Sci. Rep.* **2019**, *9*, 4345. [CrossRef] [PubMed]
32. Al-Gaashani, R.; Zakaria, Y.; Gladich, I.; Kochkodan, V.; Lawler, J. XPS, structural and antimicrobial studies of novel functionalized halloysite nanotubes. *Sci. Rep.* **2022**, *12*, 21633. [CrossRef] [PubMed]
33. Pisarek, M.; Krawczyk, M.; Hołdyński, M.; Lisowski, W. Plasma Nitriding of TiO_2 Nanotubes: N-Doping in Situ Investigations Using XPS. *ACS Omega* **2020**, *5*, 8647–8658. [CrossRef] [PubMed]
34. Cheng, C.; Song, W.; Zhao, Q.; Zhang, H. Halloysite nanotubes in polymer science: Purification, characterization, modification and applications. *Nanotechnol. Rev.* **2020**, *9*, 323–344. [CrossRef]
35. Wang, G.; Yang, J. Influences of molecular weight of epoxy binder on fire protection of waterborne intumescent fire resistive coating. *Surf. Coat. Technol.* **2012**, *206*, 4396–4404. [CrossRef]

36. Wang, G.; Yang, J. Influences of binder on fire protection and anticorrosion properties of intumescent fire resistive coating for steel structure. *Surf. Coat. Technol.* **2010**, *204*, 1186–1192. [CrossRef]
37. Zhong, F.; Lu, M.; Chen, C.; Liu, L.; Yang, X. Phytic acid cross-linked copper ions anchored to BN surface to enhance the fire performance of waterborne epoxy intumescent coatings. *Colloids Surf. A Physicochem. Eng. Asp.* **2023**, *665*, 131275. [CrossRef]
38. Zhong, F.; Zhang, X.; Wang, Y.; Li, P.; Chen, C.; Liu, L.; Yang, X. Flame-retardant properties of waterborne epoxy intumescent coatings reinforced by polydopamine@KH560/carbon nitride/graphene ternary system. *Colloids Surf. A Physicochem. Eng. Asp.* **2021**, *620*, 126506. [CrossRef]
39. Li, P.; Liu, H.; Xu, Y.-J.; Wang, D.-Y.; Liu, Y.; Zhu, P. Flame-retardant and antibacterial flexible polyurethane foams with high resilience based on a P/N/Si-containing system. *J. Mater. Sci. Technol.* **2024**, *182*, 141–151. [CrossRef]
40. Wang, B.-H.; Zhang, L.-Y.; Song, W.-M.; Liu, Y. Alkaline amino acid modification based on biological phytic acid for preparing flame-retardant and antibacterial cellulose-based fabrics. *Int. J. Biol. Macromol.* **2024**, *276*, 134002. [CrossRef] [PubMed]
41. Jiang, Q.; Li, P.; Liu, Y.; Zhu, P. Green flame-retardant flexible polyurethane foam based on polyphenol-iron-phytic acid network to improve the fire safety. *Compos. Part B Eng.* **2022**, *239*, 109958. [CrossRef]
42. Moradi Kooshksara, M.; Mohammadi, S. Investigation of the in-situ solvothermal reduction of multi-layered graphene oxide in epoxy coating by acetonitrile on improving the hydrophobicity and corrosion resistance. *Prog. Org. Coat.* **2021**, *159*, 106432. [CrossRef]
43. Liu, L.; Xia, X.; Xia, G.; Lǔ, D.; Huang, S.; Liu, K. Study on the effect of CMC/HNTs/MSN coatings on the performance of thermal transfer paper. *J. Coat. Technol. Res.* **2025**, *22*, 337–350.

Disclaimer/Publisher's Note: The statements, opinions and data contained in all publications are solely those of the individual author(s) and contributor(s) and not of MDPI and/or the editor(s). MDPI and/or the editor(s) disclaim responsibility for any injury to people or property resulting from any ideas, methods, instructions or products referred to in the content.